



OPEN Ultra-high-brightness and tuneable attosecond-long electron beams with the laser wake field acceleration

Paolo Tomassini¹✉, Federico Avella^{2,4}, Nasr A. M. Hafz³, Luca Labate², Vojtěch Horný¹, Szabolcs Tóth³, Domenico Doria¹ & Leonida A. Gizzi²

Ultra-low emittance and length-tuneable electron beams can be obtained with the Laser Wake Field Acceleration (LWFA) by employing advanced ionization injection techniques, such as the Two-Color and the Resonant Multi-Pulse Ionization injection (ReMPI) schemes. There, a tightly focused, short wavelength (ionization) pulse extracts electrons from a selected inner shell of a dopant, allowing them to be longitudinally compressed and trapped in the wakefield excited by a different (driver) pulse. In this work we demonstrate, by means of analytical results and Particle In Cell simulations, that 340 as long electron beams with 2.3 GeV energy, 6.1 pC charge, 0.15 % projected energy spread, 60 nm normalised emittance, and projected 6D-Brightness in excess of $3 \times 10^{18} \text{ A/m}^2 / 0.1\% \text{ BW}$ can be generated with a 200 TW Ti:Sa laser system. The beam slice analysis reveals its potentialities for driving a few-spikes attosecond X-ray Free Electron Laser. Furthermore, the ultra-high projected quality, and the extreme shortness of the beams make them ideal candidates for the generation of attosecond and quasi-monochromatic γ photons beams through Thomson/Compton backscattering, or for the injection in subsequent plasma wakefield structures so as to reach TeV energies from staged LWFA.

Keywords Laser wake field acceleration, High brightness electron beams, Attosecond electron beams, Free electron laser, Inverse Thomson scattering, Compton backscattering, LWFA staging

In laser-plasma accelerators working with the Laser Wake Field Acceleration (LWFA) mechanism¹, electrons are accelerated and focused by the longitudinal plasma wave excited by an ultrashort and ultra-intense laser pulse, which propagates at relativistic velocities in an underdense plasma². Due to the large accelerating electric fields (usually of the order of 100 GV/m), and therefore to their potential compactness, LWFA based accelerators are envisaged for a large variety of application, ranging from high-charge accelerators for betatron radiation generation^{3,4} aiming at high-resolution X-ray imaging⁵⁻⁷, for Very High Energy Electron (VHEE) beams generation for cancer treatment⁸⁻¹⁰, few-cycles laser pulse driven accelerators with high efficiency energy conversion for secondary particle generation¹¹⁻¹⁴, multi-pulse driven wakefield acceleration for high repetition rate sources^{15,16}, ultrashort electron beam generation for ultrafast probing¹⁷⁻²¹, high-quality accelerators for Free Electron Laser applications²²⁻²⁶, high-brilliance Thomson/Compton backscattering γ sources²⁷⁻³¹, and multi-staging for TeV energy colliders³²⁻³⁶. The latter types of accelerator are generally based upon low-emittance particle injection schemes, as the downramp injection³⁷⁻⁴⁰ with its variants⁴¹⁻⁴⁴, or on advanced ionization schemes⁴⁵⁻⁵⁰ which exploit the possibility to generate extremely cold electron beams in the transverse phase-space.

In high-quality accelerators, the normalized emittance ϵ_n , *i.e.* the measure of the (linearly) uncorrelated transverse phase space area, the energy spread $\delta E/E$ and the peak current I are the relevant figures of merit of the beam. Those parameters combine in the Beam Brightness $B_{6D} = I/(\epsilon_{n,x} \cdot \epsilon_{n,y})/(\delta E/E)|_{0.1\%}$ which expresses the compactness of the beam in the full 6D phase space, where $\epsilon_{n,x}$ ($\epsilon_{n,y}$) are the emittances referred

¹Extreme Light Infrastructure - Nuclear Physics, IFIN-HH, 30 Reactorului Street, 077125 Magurele, Romania.

²Intense Laser Irradiation Laboratory, Istituto Nazionale di Ottica, CNR, 56124 Pisa, Italy. ³The Extreme Light Infrastructure ERIC, ELI-HU Non-Profit Ltd., Wolfgang Sandner Utca 3, Szeged 6728, Hungary. ⁴“Enrico Fermi” Physics Department, University of Pisa, Largo Bruno Pontecorvo 3, 56127 Pisa, Italy. ✉email: paolo.tomassini@eli-np.ro

to the transverse phase space cuts in the x (y) directions and $(\delta E/E)|_{0.1\%} = 10^3(\delta E/E)$. Ultra-low-emittance ionization injection based schemes, such as the Two-Color⁴⁵ and the Resonant Multi-Pulse Ionization injection (ReMPI)⁴⁷, aim at generating high-brightness electron beams by using a dedicated, tightly focused and linearly polarized laser beam (a so called *ionization pulse*) which extracts electrons from selected inner shells in a gas dopant through the pulse field ionization, taking advantage of the large gap in the ionization potential between the electrons in the selected inner shell and those in outer shells. The extracted electrons can be trapped in wakefields with large enough peak longitudinal electric field⁵¹ and they will be both longitudinally and transversally compressed, thus making the generation of high-brightness beams feasible. In all the schemes described so far, the ionization pulse peak amplitude $a_0 = eA_0/m_e c^2 \simeq 0.85\sqrt{I_{18}\lambda^2/(1+\delta)}$, where I_{18} is the pulse intensity in units of $10^{18}\text{W}/\text{cm}^2$, λ is the wavelength in μm and $\delta = 0, 1$ refer to the linearly and circularly polarized cases, respectively, is tuned so as to be close to the threshold for the extraction of the first of the two electrons in the selected inner shell. This, in fact, is the condition to achieve the lowest possible residual transverse momentum after the pulse passage (and therefore the lowest emittance) for the given dopant. As the ionization pulse amplitude gets significantly higher, the saturation regime of the ionization of the first electron in the shell is reached, thus inducing a dramatic increase of the final beam emittance^{52,53}.

Both the Two-Color and the ReMPI schemes, however, need to cope with the problem of minimizing the ionization induced by the wakefield driver, which potentially generates low-quality components of the electron beam and reduces the number of available electrons to be extracted by the ionization pulse. In the Two-Color scheme, this is achieved by using a very long wavelength ($\geq 5\ \mu\text{m}$ in the original paper⁴⁵) driver pulse, while ReMPI relies on a longitudinal tailoring of the driver as a train of resonantly delayed sub-pulses, each of them having the amplitude below the threshold for the ionization of the dopant (eight sub-pulses with a standard Ti:Sa system in the original paper⁴⁷ or four sub-pulses in⁴⁹). Both schemes have been numerically proven to be capable to generate very low emittance beams. Technical issues for the generation of ultrashort, high intensity and long wavelength laser pulses, as well as the complexity of the setup required to generate a stable train of eight or four pulses, make the experimental demonstration of both schemes challenging.

Here we present and test, by means of analytical models and high-fidelity Particle In Cell (PIC) simulations, a novel and experimentally easier to implement ReMPI configuration. This layout relies on a stable generation of a two-pulse driver by means of a multi-ring delay mask, and on the selection of the driver intensity ensuring a dark-current free-electron beam with outstanding transverse emittance. Results show that electron beams having energy in excess of 2.3 GeV, projected energy spread of 0.15% *rms* from Gaussian fit, normalized emittances $\epsilon_{n,x} = 90\ \text{nm}$ (ionization pulse polarization plane), $\epsilon_{n,y} = 32\ \text{nm}$ and 6D-Brightness of $3.4 \times 10^{18}\ \text{A}/\text{m}^2/0.1\%\text{BW}$ can indeed be generated in a stable way by employing a 200 TW class Ti:Sa laser system. In particular, the duration of these beams can be fine-tuned, with a minimum duration and charge of 340 as and 6.1 pC/shot, respectively. Beside the application of these electron beams in multi-stage acceleration, a Free Electron Laser generating sub-fs single-spike coherent X radiation^{54–56}, or a quasi-monochromatic sub-fs 10's MeV gamma ray beams generation through quasi-linear Thomson/Compton backscattering^{29,30,57,58} can be envisaged as applications of this new electron beam source.

Results

Layout for a stable ReMPI configuration

The proposed layout of the LWFA accelerator enforcing the ReMPI scheme is shown in Fig. 1. A 200 TW-class laser pulse from a Ti:Sa system (4.6 J in 23 fs after the compressor) is split into three components by using a multi-ring delay mask with a mirror in the inner core (A;C) (see the *Materials and Methods* section). The multi ring structure in the delay mask generates two multi-ring structured pulses, separated by a time delay of 151 fs, which corresponds to the plasma oscillation period for the working plasma density of $n_0 = 5 \times 10^{17}\ \text{cm}^{-3}$. The double pulse is converted in circular polarization via a $\lambda/4$ plate and focused on the target through an F/38 off-axis parabola, thus resulting in a double pulse having a $w_{0,d} = 30\ \mu\text{m}$ waist, with a transverse structure very similar to those obtainable with supergaussian shaped pulses in the near field. The inner part of the main pulse is reflected by the mirror of 16 mm diameter and subsequently frequency tripled with LBO and BBO crystals, resulting in a $< 30\ \text{fs}$ long pulse of 270 nm wavelength, delivering $> 60\ \text{mJ}$. After passing through a delay line (c3), the frequency tripled pulse acting as the ionization pulse, is expanded in diameter via a telescope (c4) and focused on the target down to a spot of waist $w_{0,i} = 3.5\ \mu\text{m}$ through an F/13 parabola and a mirror equipped with a hole (c5). The full characterization of the ionization pulse generation and focusing is shown in *Materials and Methods* and in the *Supplementary Materials* document.

The target is made up by a two-sections preformed plasma waveguide (such as a capillary discharge^{59–64} or a HOFI plasma channel^{65–69}), the first one (2 mm long) being filled with pure Argon and having a plasma density of $5 \times 10^{17}\ \text{cm}^{-3}$ and the second one (30 mm long) filled with Helium, with a smooth 2 mm long electron density transition between the stages having a 30% increase with respect to the first one. A standard radial parabolic plasma density profile, so as to keep the driving train guided and focused⁷⁰, is supposed to be present for the whole target length of 3.4 cm. The first stage is devoted to the extraction and trapping of the inner shell electrons from the Argon ions, namely through the tunnel ionization process starting from Ar^{9+} . There, the focused driver train (in circular polarization) and the ionization pulse (in linear polarization) reach normalized amplitudes $a = eA_{\perp}/m_e c^2$ of $a_{0,d1} = 0.810$, $a_{0,d2} = 0.886$ and $a_{0,i} = 1.150/3$, respectively. In the current configuration, the wakefield is moving with a phase speed $v_{\phi} = c\beta_{\phi}$ whose relativistic Lorentz factor is $\gamma_{\phi} \simeq (n_c/n_0)^{1/2} = k_l/k_p \simeq 58$, where k_l is the driver pulses wave-vector, $k_p = (4\pi n_0 e^2/m_e c^2)^{1/2}$ is the plasma wave-vector for the plasma wavelength of $\lambda_p \simeq 47\ \mu\text{m}$ and $n_c = m_e c^2 k_l^2/4\pi e^2$ is the critical density for the driver pulses. The nonrelativistic wave-breaking limit (or Dawson field) is $E_{0,p} = m_e c^2/ek_p \simeq 70\ \text{GV}/\text{m}$.

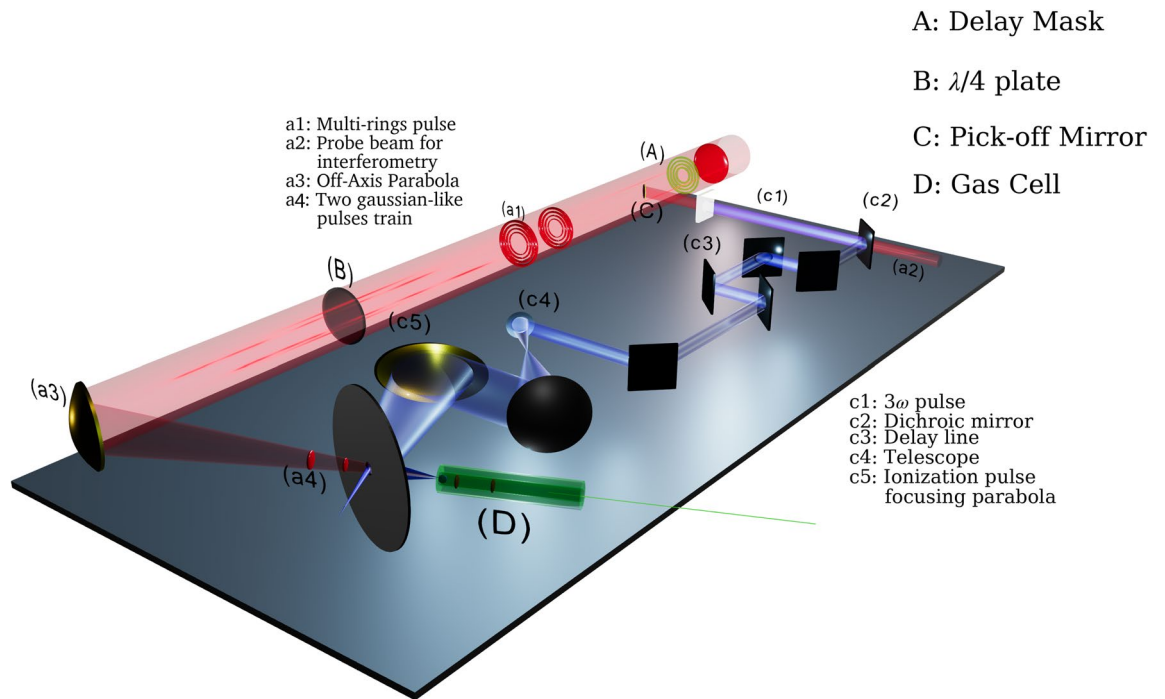


Fig. 1. Schematic setup of the proposed two-driver pulses ReMPI scheme. An ultraintense pulse from a Ti:Sa system is spatially and temporally split by using an in-built multi-ring delay mask with a mirror in the inner core (A). The multi ring structures in the delay mask generates two multi-ring structured pulses (a1), separated by a time delay given by the plasma oscillation period for the working plasma density. The double pulse is converted in circular polarization via a $\lambda/4$ plate (B) and focused on the target through an F/38 off-axis parabola (a3). The inner part of the main pulse is reflected by the pick-off mirror (C) and frequency tripled with LBO and BBO crystals. After passing through a delay line (c3), the *ionization pulse* is expanded in diameter via a telescope (c4) and focused on the target through a dedicated F/13 parabola and a mirror with a hole (c5).

Particle extraction and trapping for dark-current free beams

Particles extraction and trapping in the plasma wave are crucial and deeply interconnected processes which must be finely tuned in order to obtain high quality and dark-current free beams, *i.e.* electron beams without particles injected by unwanted and competing mechanisms (see *e.g.* Ref.⁷¹), which usually spoil out the beam quality. Here, the electrons constituting the accelerated beams are extracted *via* tunnel ionization^{72–74} from L inner shell electrons of Argon atoms residing in the first target section, while the background plasma electrons comprises either the outer Argon electrons in the first section or both the He electrons in the second accelerating section. As it will be apparent below, in the proposed working configuration only the electrons extracted by the ionization pulse will be trapped by the plasma wave, thus obtaining charge- and length-tuneable beams with ultra low-emittance.

The electric field associated to the driver pulses is responsible for the full extraction of the Argon outer electrons up to the 7th (having ionization potential $U_I \leq 143$ eV), for an almost full extraction of the first electrons in the L-shell ($Ar^{8^+ \rightarrow 9^+}$, with $U_I = 422.45$ eV) and for a partial extraction of the second electrons in the shell ($Ar^{9^+ \rightarrow 10^+}$, with $U_I = 479.69$ eV), while no electron from the $Ar^{10^+ \rightarrow 11^+}$ (with ionization potential of $U_I = 538.96$ eV) is extracted by the driver pulse. Remarkably, the design of the working configuration was tailored so that the initial conditions of those inner electrons were not yet favorable for particle's trapping in the plasma wave, thus making them an additional component of the plasma electrons and enabling for the generation of dark-current free beams. This is apparent with the inspection of Figs. 2 and 3, were a snapshot at $t = 2.103$ ps of the q-3D PIC simulation referring to the proposed working point parameters are shown. At that time, the pulses propagated into the first section filled with Argon and the ionization pulse reached its focus point. In Fig. 2 the 3D structure of the longitudinal electric field is shown, along with the pulses envelope, highlighting that the wakefield is resonantly excited by the two drivers beam and the plasma dynamics is far from the blow-out regime⁷⁵. Therefore, simplified trapping conditions based on the quasi-static evolution⁷⁶, longitudinal particle dynamics and on-axis line-out of the fields can be made. The analysis of the trapping condition confirms the results from PIC simulation, showing the absence of trapped electrons when the ionization pulse is not included (see the *Materials and Methods* section)

High-brightness GeV 340 as long e-beams generation

After the extraction and injection of the particles in the first target section, which leads to an ultrashort and dark-current free ultra-low emittance 6.1 pC beam, an adiabatic rephasing which moves the electrons in the

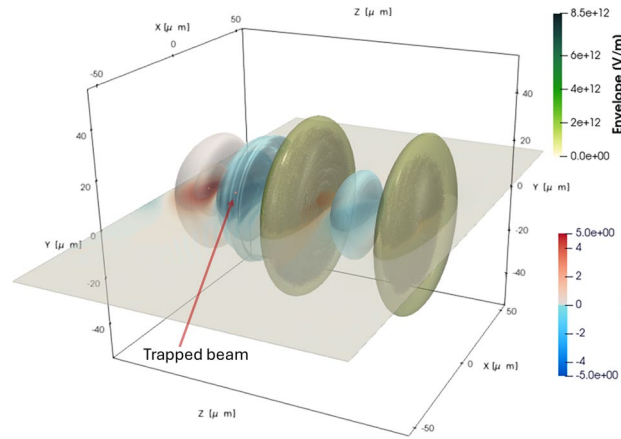


Fig. 2. Three dimensional view of the wake field and of the accelerated beam at time $t = 5.3$ ps, where the beam just left the injection section and it's entering the accelerating structure's plateau. The accelerating field is resonantly excited by the two drivers pulses (in green). The trapped beam (in red) is lying in the negative E_z region as indicated by the arrow, while the portion of the beam that will be expelled by the plasma wake is lying in the positive E_z region.

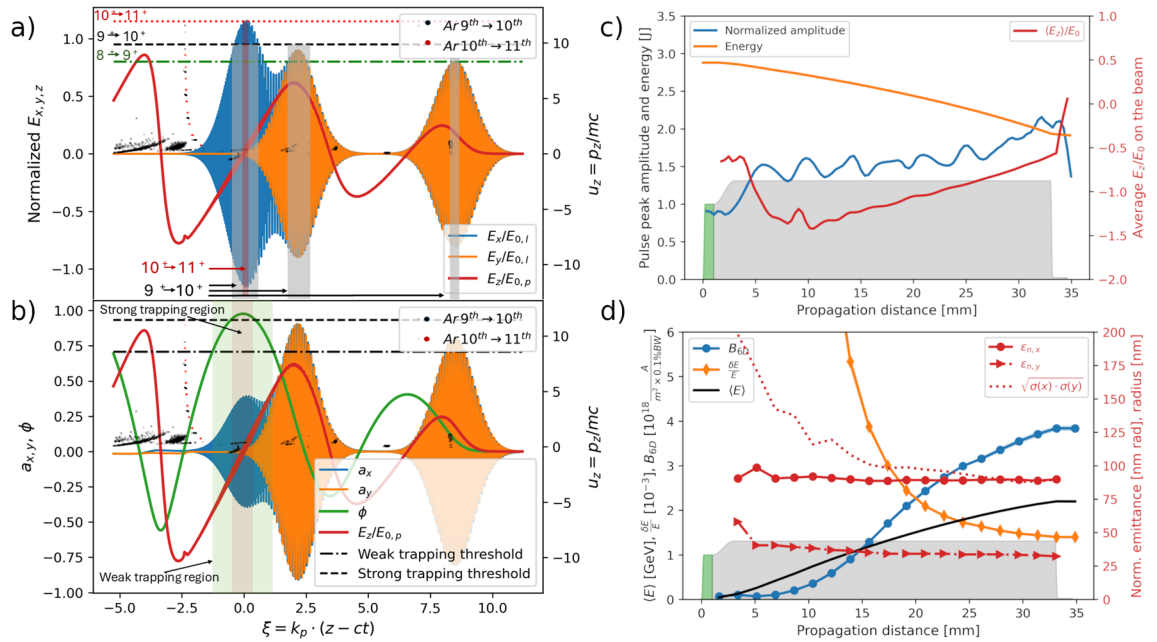


Fig. 3. Trapping conditions for the electron beam. Snapshot of the fields and longitudinal phase-space of the extracted electrons at simulation time $t = 2.103$ ps, where the pulses are at their focus point in the center of the first target section. In panel (a) the particles extraction is depicted along with the on-axis line-out of the normalized electric fields components. The horizontal dashed-dot green line represents the saturation threshold for the extraction $Ar^{8^+ \rightarrow 9^+}$ from the driver pulses. The black and red dashed line show the saturation threshold for $Ar^{9^+ \rightarrow 10^+}$ and $Ar^{10^+ \rightarrow 11^+}$ from the ionization pulse, respectively. The vertical gray and red bands show the approximate original position of the $Ar^{9^+ \rightarrow 10^+}$ and $Ar^{10^+ \rightarrow 11^+}$ extracted electrons. In panel (b) the trapping condition is emphasized. There, the normalized potentials and the accelerating gradient are shown. The available extraction region which allows for further *weak* (*strong*) particle trapping is emphasized with the vertical green (red) band. As a combined result, only the electrons extracted by the ionization pulse will be further accelerated. (c) and (d) Fields and electron beam evolution along target. The first and second sections density profiles are shown in green and gray, respectively. (a) Total pulse energy (orange) and peak normalized evolution (blue). The right (red) axis shows the evolution of the averaged normalized longitudinal electric field on the beam $\langle E_z \rangle / E_0$. (b) Electron beam average energy (black), rms energy spread (orange) and brightness 6D (blue) evolution. The right (red) axis shows purely transverse quantities as the normalized emittances along x and y as (full lines) long as the beam transverse size (dashed line).

rear of the bucket is obtained *via* a monotonically increasing density interface connecting the injection and the acceleration stages. Thanks to the maintained transverse matching condition along the beam propagation, the ultra-low beam emittance is preserved in this transition^{77–79}. During their propagation in the plateau of the second stage, the guided driver pulses smoothly increase their peak amplitude (see Fig.3c), thus exciting a wakefield in a quasi-blowout regime. This assures the presence of a transversely linear force with constant shape within the bunch, therefore suppressing the emittance dilution inside the accelerating structure (see Fig.3d). The inspection of Fig.3d also reveals the expected radial shrinkage of the matched beam (dashed red line) as $\sigma_{tr} = \sqrt{\sigma(x) \times \sigma(y)} \propto \gamma^{-1/4}$ up to the end of the target plateau⁷⁹. The average beam energy (black line) increases less than linearly with the propagation distance as the electric field on the beam starts decreasing after 10 mm of propagation, with a final average beam energy of 2.3 GeV. As the beam current remains constant after the trapping point and the transverse emittance is stable along all the beam propagation, the resulting 6D-Brightness (blue line) simply evolves as the inverse of the beam energy spread (orange line). We mention *stat*, due to the presence of long tails in the beam, both the beam duration and energy spread are evaluated with *robust statistics* methods and expressed in their equivalent *rms* values.

At the end of the density plateau the *rms* energy spread and normalized emittances are $\delta(E)/E = 0.14\%$, $\epsilon_{n,x} = 90$ nm and $\epsilon_{n,y} = 32$ nm, respectively. Notably, the beam quality is preserved during the 0.2 mm long downramp, being the final energy spread unchanged and being the final emittances of $\epsilon_{n,x} = 91$ nm and $\epsilon_{n,y} = 32$ nm only barely affected by the mismatched transverse fields. The design of an optimized downramp profile, to match a dedicated beam transport line for a specific usage of the electron beam (see *e.g.*⁴⁹ for a similar case with a multi-pulse driver), is out of the scope of the present work. Projections of the final beam 6D shape are shown by Fig.4. In panel a) the particles energy as a function of the longitudinal (z) coordinate and the x coordinate is shown, with (macro) particle coloring according to their relative weights. There, the presence of a beam bulk and of a long, low charge, tail with an position-energy correlation is apparent also by inspecting the z -energy projection in the same panel. In panels b)-d) the particle coloring is linked to their energy. In panel b) the full-3D beam shape is shown, thus confirming the quasi-cylindrical transverse shape and the presence of an higher energy tail. In panel c) the transverse phase space $x - u_x$ versus the longitudinal coordinate of the diverging beam is shown, while in panel d) the diverging properties in the x and y directions can be inferred by exploiting the monochromaticity of the beam.

More detailed information about the beam quality can be obtained by performing the slice analysis of the final 6D phase-space, also in view of a possible usage of the beam to drive a Free Electron Laser (FEL). As the evaluation of the FEL performance of the beam is out of the scope of the present work, we limit ourself to a slice analysis with a reasonable slice thickness of 20 nm, which is compatible with a FEL operating at 3 nm and having a Pierce parameter $\rho_{FEL,1D} = 5 \times 10^{-3}$, with a coherence length^{80–83} of about 30 nm, the latter being evaluated after the dimensioning of the main FEL parameters. We stress that the validity of the basic SASE-

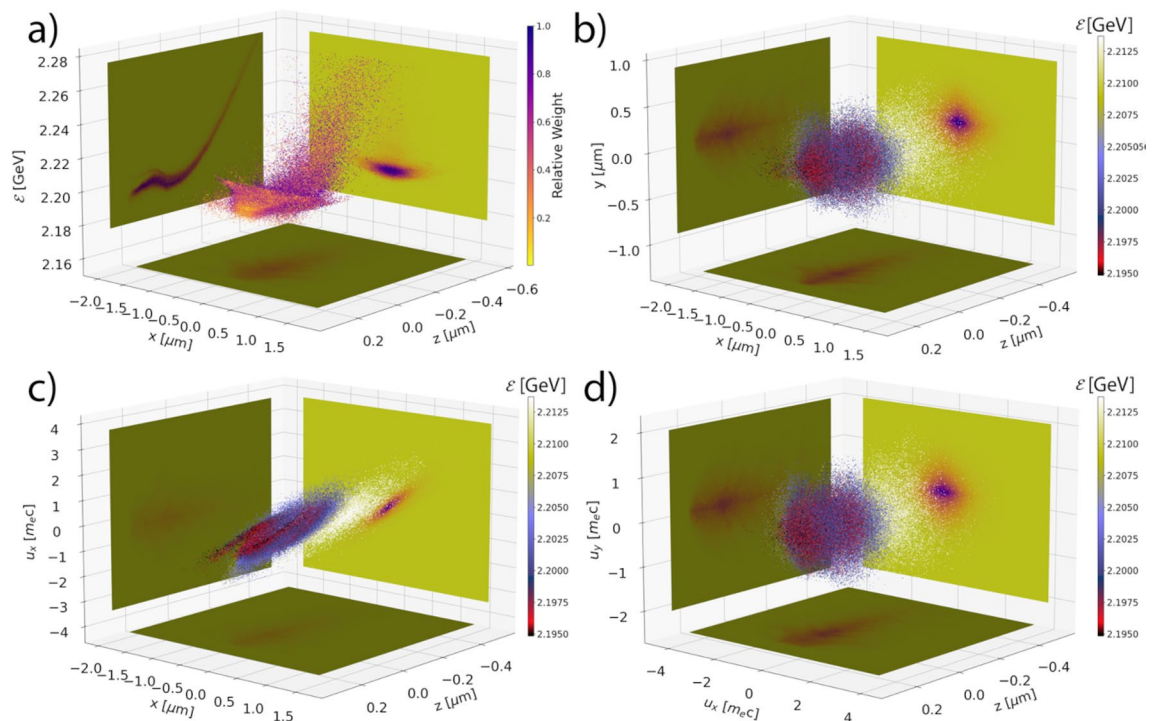


Fig. 4. 6D phase space cuts of the electron beam after the plasma exit. **(a)** Energy vs the longitudinal (z) and transverse (x) position. The macroparticles are colored according to their relative weights **(b)** 3D spatial distribution. **(c)** Normalized momentum $u_x = p_x/m_e c$ vs z and x positions and **(d)** full transverse momenta u_x, u_y vs z . In **(b, c, d)** the macroparticles are colored according to their energy.

FEL⁸¹ formulae is questionable for such an ultrashort electron beam, being the coherence length and the *rms* duration of similar sizes, therefore leading to the necessity of a full chain of start-to-end simulations for the FEL dimensioning.

Figure 5 shows the slice analysis of the final beam. The beam current (black line) reaches the peak value of 13 kA, with asymmetric profile showing a long tail. The FWHM duration of the current profile is $T_{FWHM} = 0.835$ fs, which is equivalent to the *rms* duration of 355 as, in good agreement with the value of 340 as obtained by curve fitting of the particles longitudinal distribution. Remarkably, inside the beam bulk the energy spread (blue line) is limited to the interval $1.00\text{--}1.25 \times 10^{-3}$, with higher values in the long and tenuous tail. The 6D-Brightness (green line) reaches the peak value of $B_{6D} = 5.1 \times 10^{18} \text{ A/m}^2/0.1\% \text{ BW}$ on the head of the beam, where both the energy spread and the emittances are lower and the current is of about 5 kA. Notably, around the peak current, the brightness steadily exceeds the value $B_{6D} = 3.5 \times 10^{18} \text{ A/m}^2/0.1\% \text{ BW}$.

The right (red) axis in Fig. 5 shows the normalized emittances along *x* (hash-dot line) and *y* (dot line). There, the deviation of the slice energy from the average beam energy (red full line) is also shown. The slice energy deviation from the average, encoding the longitudinal non-uniformity of the beam energy, is expressed in the form $\delta\gamma \equiv (\gamma/\langle\gamma\rangle - 1) \times 10^3$ and is related to the so called position-correlated energy spread. We note now that $\delta\gamma$ is almost perfectly flat in the beam bulk, while the non-flat region is related to the low-current tail. This enables the possibility to achieve an ultra-low (projected) energy spread beam. Moreover, the slice relative energy spread measures the *rms* departures of the sliced beam energy from the local (slice) average energy, thus defining a curved band within which the particles energies are likely to be found. The red band in the $\delta\gamma$ curve (related to the right axis), with lower and upper bounds of $\delta\gamma - 2\sigma(E)/E$ and $\delta\gamma + 2\sigma(E)/E$, respectively, highlights the region within which the 95.45% of the electrons are found. The orange band shows the region of the beam where 95.45% the particles energy doesn't change more than $\pm 0.25\%$. Remarkably, the region of almost uniform particles energy extends for the large majority of the beam core and it includes about 80% of the beam charge, thus making the beam of interest for FEL applications.

Tuneable sub-fs long beams generation

As pointed out in a previous work²¹, the usage of a dedicated ionization pulse as in the ReMPI or in the Two-Color schemes (for LWFA) and in the plasma-photocathode scheme (for PWFA⁸⁴), can lead to the generation of ultrashort pulses with tuneable lengths. Beam durations well below the femtosecond level can be achieved when i) the wakefield is stable during the whole beam extraction time, ii) the tightly focused ionization pulse is placed in the vicinity of the node of the longitudinal accelerating gradient, iii) the longitudinal and transverse beam momenta after the pulse slippage are very small and iv) the trapped beam is placed in a region with a large longitudinal electric field²¹. In quasilinear regimes, the latter condition is fulfilled when the *strong trapping* condition is reached, which explains why the working conditions for the proposed accelerator were tuned so as to reach the quasi-linear regime with enabled strong-trapping in the early stage of beam extraction and trapping. Under the conditions listed above, the *rms* beam length after trapping $\sigma(\delta z_t)$ can be evaluated by means of the ionization pulse length $L_i = cT_i/\sqrt{\log(4)}$, the distance \bar{z}_e of the ionization pulse center to the accelerating field node, the longitudinal gradient $\partial_\xi \hat{E}_z^e = \frac{\partial}{\partial k_{pz}} E_z/E_{0,p}|_e$ of E_z at the extraction, the radial gradient of the

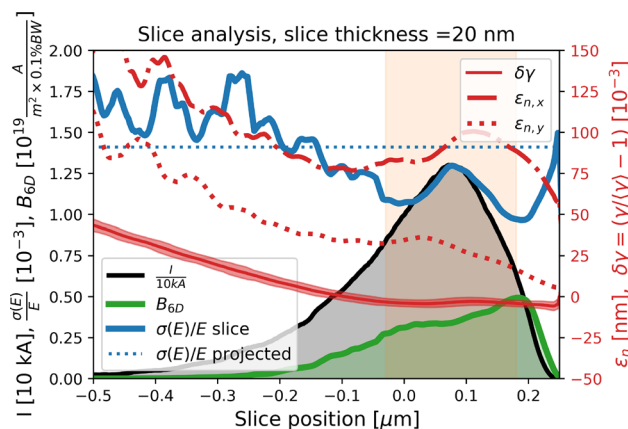


Fig. 5. Slice analysis of the final electron beam, with slice thickness of 20 nm. The current (black line) reaches the peak value of 13 kA. The energy spread (blue line) is limited in the interval $1.0\text{--}1.25 \times 10^{-3}$ inside the beam bulk. The 6D-Brightness (green line) exceeds $3.5 \times 10^{18} \text{ A/m}^2/0.1\% \text{ BW}$ at the current maximum, and reaches the peak value of $5.1 \times 10^{18} \text{ A/m}^2/0.1\% \text{ BW}$ on the head of the beam, where both the energy spread and the emittances are lower. On the right (red) axis the normalized emittances along *x* (hash-dot line) and along *y* (dot line) are shown. The right axis also shows the deviation of the slice energy from the average beam energy (red full line) expressed in 10^{-3} as $\delta\gamma = (\gamma/\langle\gamma\rangle - 1) \times 10^3$. The upper and lower bounds of the red band encode the local energy spread $\sigma(E)/E$, and are evaluated as $\delta\gamma + 2\sigma(E)/E$ and $\delta\gamma - 2\sigma(E)/E$, respectively. The orange band shows the region of the beam where the particles energy does not change more than $\pm 0.25\%$.

radial electric field at the extraction $\partial_{k_p r_e} \hat{E}_r^e = \frac{\partial}{\partial k_p r} E_r / E_{0,p}|_e$, and the longitudinal electric field at trapping $E_z^t = E_z / E_{0,p}|_t$ through the following relation:

$$\sigma(\delta z_f) \gtrsim \frac{k_p \rho_0}{\sqrt{2} E_z^t} \left\{ (\partial_\xi \hat{E}_z^e)^2 \left[\frac{1}{4} + \left(\frac{\bar{z}_e}{\sqrt{\rho_0} L_i} \right)^2 \right] L_i^4 + (\partial_{k_p r_e} \hat{E}_r^e)^2 w_{0,i}^4 \right\}^{1/2} \tag{1}$$

We acknowledge here that Eq. 1 is Eq. 11 of Ref.²¹ after the substitution $\rho_0^2 = \Delta$ and the amendment from a typesetting error on the power of E_z^t .

The analysis of the electric field map during the beam extraction and trapping is shown in Fig. 6. We mention that the field gradients differ from the ones that can be inferred by analytical theories in the full blow-out regime (see *e.g.*⁸⁵), as a partial cavitation of the plasma electrons behind the second driver pulse was reached. In panel a) the on-axis line-out of the normalized accelerating gradient (black line) shows a steady longitudinal electric field gradient around $\xi = k_p(z - ct) = 0$, with $\partial_\xi \hat{E}_z^e = \frac{\partial}{\partial k_p z} E_z / E_{0,p}|_e = 0.36$. The longitudinal extraction regions for the cases of ionization pulse phase $\bar{\xi}_e \equiv k_p \bar{z}_e$ placed on the node of the accelerating gradient ($\bar{\xi}_e = 0$), or centered with a distance from the node of 3 μm ($\bar{\xi}_e = -0.4$) are shown in blue and orange, respectively. Notably, the trapping positions for the two ionization pulse position cases of $\bar{\xi}_e = 0, -0.4$ are very close and placed around the peak of E_z (see the vertical dashed lines). The two trapping positions $\bar{\xi}_t = -2.24, -2.28$, which are inferred by using the potential $\phi(\xi) = -\int^\xi \hat{E}_z^e$ (red line) and the trapping relations $\phi(\bar{\xi}_t) = \phi(\bar{\xi}_e) - 1 + 1/\gamma_\phi$, are consistent with the beam position inferred from the beam loading effect, which is visible in the same position. The longitudinal gradient at the trapping points is $\hat{E}_z^e \simeq -0.72$. In panel b) of the same figure, the transverse line-out of the radial electric field at $\xi = 0$ is shown. The field exhibits

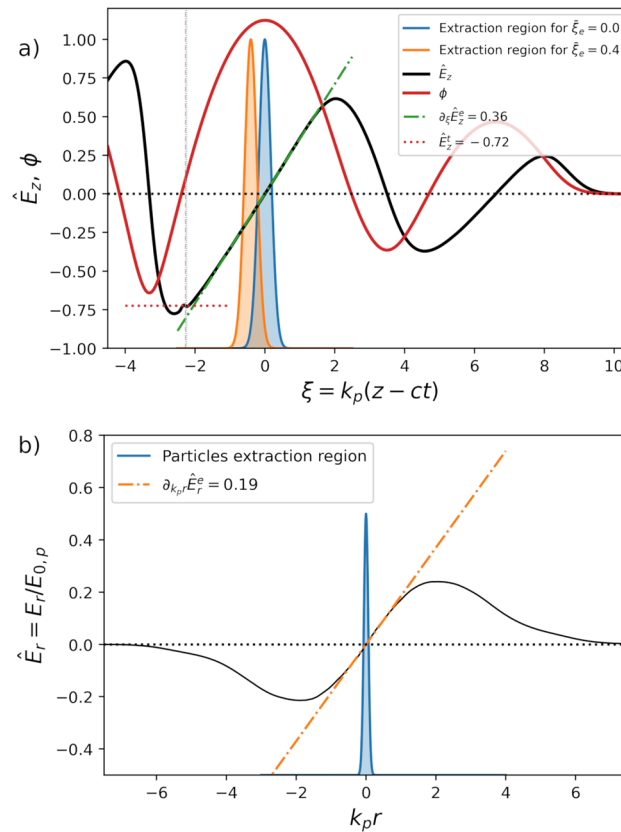


Fig. 6. Electric field and potential at the beam trapping point. **(a)** On-axis line-out of the normalized accelerating gradient (black line). The longitudinal extraction regions for the cases of ionization pulses centered on the node of the accelerating gradient ($\bar{\xi}_e = 0$) and on $\bar{\xi}_e = -0.4$ are shown in blue and orange, respectively. The trapping positions for the two cases are inferred by using the potential $\phi(\xi)$ (red line), leading to $\bar{\xi}_t = -2.24, -2.28$, respectively (see the almost overlapping vertical dashed lines). **(b)** Transverse line-out of the radial electric field at $\xi = 0$. The field is linear around the axis, with gradient $\partial_{k_p r_e} \hat{E}_r^e = \frac{\partial}{\partial k_p r} E_r / E_{0,p}|_e \simeq 0.19$. The radial extent of the extraction region is shown in blue.

a linear radial dependence well beyond the radial extent of the extraction region (shown in blue), with gradient $\partial_{k_p r_e} \hat{E}_r^e = \frac{\partial}{\partial k_p r} E_r / E_{0,p}|_e \simeq 0.19$.

With the given synthetic field parameters of $\partial_{\xi} \hat{E}_z^e = 0.36$, $\partial_{k_p r_e} \hat{E}_r^e = 0.19$ and $E_z^t = 0.72$, the estimated beam length is a function of the $\bar{z}_e = \xi_e / k_p$ solely, which is easily tuned by changing the delay $\Delta t = -\bar{z}_e / c$ between the ionization pulse and the driver train. For simplicity, we will refer to a delay $\Delta t = 0$ when the ionization pulse is placed on the node of the accelerating gradient. The results of a set of PIC simulations operated by changing Δt are shown in Fig. 7 (black line). There, the *rms* duration obtained by fitting is almost perfectly matching the estimated values obtained with the model of Eq. 1 (blue full curve), the band interval being related to the durations which can be reached with ionization pulses duration between 20 fs and 40 fs. We notice that the model underestimates the beam durations when $|\Delta t| \ll 5$ fs, *i.e.* when beam-loading effects due to the very large current play a relevant role during the trapping. Moreover, the model underestimates the beam duration when $\Delta t < -5$ fs, too. In this case the ionization pulse is close to the driver pulse, which results in an increased transverse momentum spread and more distributed trapping positions.

The results shown above refer to the tuneability of the beam duration. However, as the beam center of mass position, the current peak value and actual shape also depend on Δt , the beam-loading effect which minimizes the final energy spread should be obtained by optimizing the extracted charge, too. Therefore, for any given delay Δt , there exist an optimal trapped beam charge and acceleration length which minimize the final energy spread. This optimization procedure is out the scope of the present work, as we aim at generating the shortest possible electron beam with the present configuration. However, we mention that in an earlier work with the ReMPI scheme driven by eight pulses from a PW-class Ti:Sa system, the optimization for a longer electron beam (about 2 fs) resulted in a 5 GeV beam with 30 pC charge and minimum slice energy spread at the peak current of 0.05%⁵⁰.

Stability of the LWFA accelerator

A partial robustness analysis of the proposed scheme with the current working point shows that stable electron beams can be generated when i) the temporal jitter between driver-ionization pulses is maintained below a few femtoseconds *rms*, and ii) the background density variations and the laser pulses intensities fluctuations are maintained at a percent level. Robustness against transverse pointing fluctuations is not included in the present work, as it is strictly dependent on the actual target and laser-guiding structure (capillary, exact HOFI channel radial profile, plasma discharge). Therefore, here we will evaluate the variation of the final beam quality by introducing small fluctuations in the background plasma density n_0 ($\pm 1\%$), in the incoming laser pulse amplitude a_0 ($\pm 1\%$), corresponding to $\simeq \pm 2\%$ in energy, and in the temporal jitter between the ionization and the driver pulses. The latter information, as discussed in the previous paragraph, has to be meant as a pure time jitter effect, the configurations with $|\Delta t| > 0$ not being subject to any further individual optimization processes.

Results from simulations with parameters as in the selected working points but each with a single modified Δt , background density or incoming pulse energy, are shown in Fig. 8, where the values of the beam synthetic parameters are expressed as a fraction of the ones obtained in the nominal working point. In panel a) the dependence of the beam duration, energy spread, normalized emittance $\epsilon_n = \sqrt{\epsilon_{n,x} \times \epsilon_{n,y}}$ and 6D-Brightness are shown as a function of the jitter Δt between the ionization and driver pulses. There, the sizable beam degradation for $|\Delta t| \gtrsim 2$ fs is apparent, thus implying that the time stabilization between the driver train and the ionization pulse should be maintained at the femtosecond level *rms*. Being both the pulses extracted by the same initial beam, the time jitter between them will be mostly generated by micro-vibrations, which can usually be maintained below the μm size. In panels b-d) a scenario in which six consecutive (simulation) shots that mimic

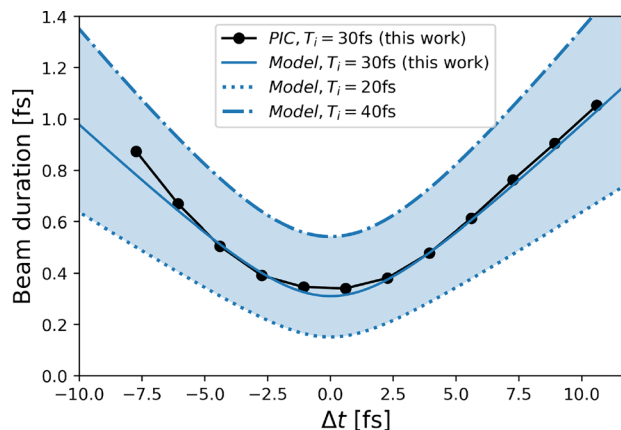


Fig. 7. Dependence of the beam duration from the delay $\Delta t = -\bar{\xi}_e / (k_p c)$ between the ionization pulse center of mass and the node of the accelerating gradient, where the beam lengths are expressed in *rms* equivalent and evaluated with the robust MAD statistics. The solid lines refer to working points having ionization pulse duration $T_i = 30$ fs FWHM, as in this work. The blue band corresponds to the interval of durations achievable with ionization pulses having duration between 20 and 40 fs long.

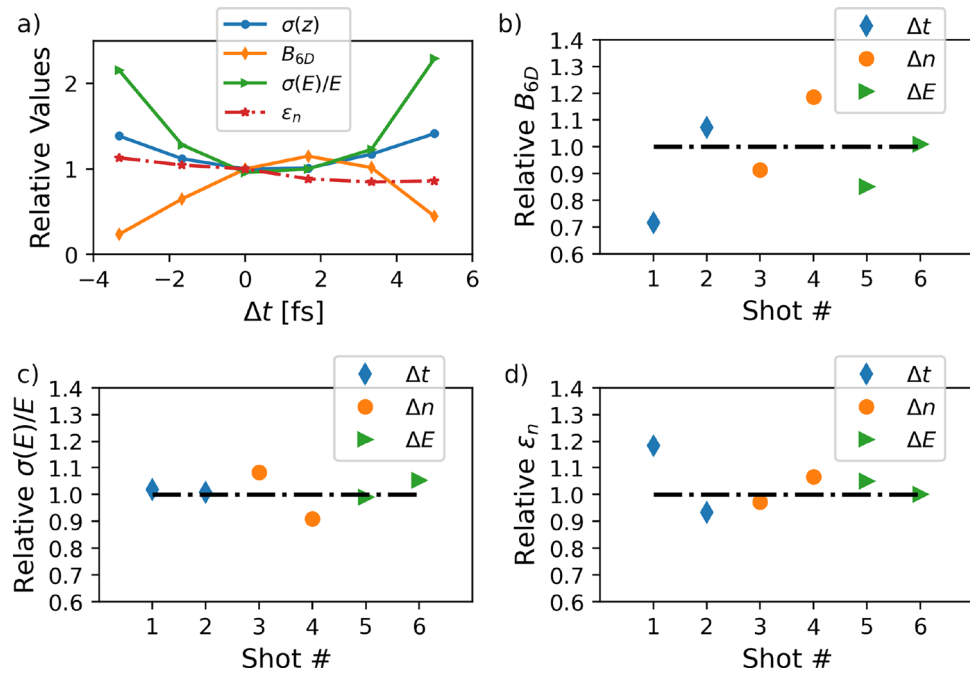


Fig. 8. Stability analysis against shot-to-shot ionization-driver time jitter (Δt), background density variation (Δn) and incoming pulse delivered energy (ΔE). The synthetic beam quality parameters are expressed as a ratio to their values at the nominal working point. **(a)** Ionization-to-driver pulses jitter scan. **(b)–(d)** Sequence of six simulations with variation in Δt (blue diamonds), variation in n_e (orange circles) and variation in pulse energy (green triangles).

the presence of the analyzed fluctuations are shown, referring to the variation of the 6D-Brightness, the energy spread and the emittance. We stress that, being the driver train made up by only two pulses, the background density fluctuations generate tiny fluctuations of the peak electric field ($\delta E_{max}/E_{max} \approx \frac{1}{2} \delta n/n$), while they induce variations of the ionization pulse position with respect to the accelerating gradient node, therefore acting as an equivalent time jitter $\Delta t|_{equiv} \simeq \frac{1}{2} \delta n/n(L/c)$, being $L \gtrsim 2\lambda_p$ the spatial distance between the ionization and the driver pulses. As a result, density fluctuations of 1% induce almost negligible variations in the electric field peak, while they introduce an equivalent time jitter of $\Delta t|_{equiv} \simeq 1.7$ fs. In each of the panels b)-d) the sequence of shots is organized as two time jitter variation with $\Delta t = \pm 1.5$ fs (blue diamonds), two density fluctuation with $\Delta n/n = \pm 1\%$ (orange circles) and two pulse energy fluctuation with $\Delta E/E = \pm 2\%$ (green triangles). The sequence of simulation shots shows that both the energy spread and the emittance are pretty stable, having $\approx 10\%$ variability, while the 6D-Brightness fluctuations are of $\approx 20\%$, meaning that the variation in the beam current and in the quantity $\epsilon_n^2 \sigma(E)/E$ are not proportional, as confirmed by the inspection of panels c) and d). We finally stress that, due to the fact that the accelerated beam is very short and that it lies in the second wakefield bucket, its longitudinal beam quality is more sensible to density fluctuations than in standard LWFA accelerators working in the first accelerating region and with femtosecond-long beams. This leads to a projected energy spread increase in excess of 20% in the case of plasma density fluctuations of $\pm 2\%$.

Discussion

A novel and reliable scheme to generate duration-tuneable (with a minimum of a few hundreds attoseconds) and ultra-high-brightness beam, with 6D-Brightness surpassing by at least two orders of magnitude the one obtained in previous studies for GeV scale beams^{86,87}, was proposed and tested with high-fidelity PIC simulations. Such a scheme is based upon the Resonant Multi-Pulse Ionization injection concept⁴⁷, and employs an innovative method to tailor in a reproducible way the time duration of the driver beam into two sub-pulses (see "Generation of the driver pulse train" in *Materials and Methods*). The usage of only two pulses of the driver, which drastically simplifies the experimental realization of a stable accelerator still maintaining the possibility to obtain high-brightness beams, was made possible by a deep analysis of the electron extraction process and of the subsequent particle dynamics in the laser field. This analysis led to the introduction of a new working point in which the base ionization level of the Argon L-shell is totally saturated by the driver pulse (see "Trapping analysis for dark-current free beams" and "Minimum achievable emittance and saturation effects" in the *Materials and Methods* section).

The optimized working point presented here is based upon a widely available 200TW Ti:Sa laser system and leads to > 2 GeV energy beams with projected energy spread of 0.15%, normalized emittance well below 100nm and slice quality compatible with Free Electron Laser requirements. Since the only optical components needed for the laser beam time shaping is the multi-ring phase-mask, the scheme is potentially scalable to PW-level laser system, thus being of interest for multi-GeV FEL-oriented LWFA facilities as EuPRAXIA²⁴, or to

multi-PW laser system as in ELI-NP⁸⁸, ELI-BL⁸⁹, Apollon⁹⁰, SuLF⁹¹ and in a near future to OPAL^{92,93}, to generate multi tens of GeV high brightness and ultrashort beams for nonlinear QED studies^{94,95} and brilliant Nonlinear Compton sources^{96–98}.

A detailed setup, which includes the beam-propagation simulations for beam shaping and the generation of the laser pulse converted in third harmonics with its subsequent focusing, was also presented (see "Ionization pulse generation and focusing" in *Materials and Methods* and in the *Supplementary Materials*), thus showing the feasibility of the proposed scheme. The plasma target was considered as having a standard parabolic transverse profile. The description of the generation of such a standard profile was out of the scope of the present work, and will be subject of future works devoted to the actual implementation of the scheme in a specific facility. A set of additional simulations, devoted to the study of the electron beam stability against fluctuations of the laser and target parameter, remarkably showed that the scheme is robust towards ionization-to-driver time jitter, plasma density fluctuations and laser pulse delivered energy fluctuations, provided that the former is confined within a few femtoseconds *rms* and the others within a percent level. As both the ionization and the driver pulses originate from the same laser pulse, only micro-mechanical vibration can introduce the time jitter between them, thus easing jitter stability condition. Moreover, as in the present configuration only two driver pulses are necessary, a less stringent upper limit for the plasma density fluctuation than in⁴⁹ is necessary to assure the beam stability. The full stability analysis, which also includes transverse pointing fluctuations, was out of the scope of the present work as it is strictly related to the actual implementation of the channel guiding technique, also usually leading to deviations from the parabolic plasma profile.

The full experimental implementation of the scheme is demanding in terms of mechanical stability and can be obtained in a well controlled environment, with micro-vibrations well below the μm level *rms*. The target design, which includes the radial shaping for the driver pulses guiding and the smooth plasma density transition between the injection and the acceleration stages, is a critical component, although its limited length reduces the complexity of maintaining a longitudinally flat profile. Therefore, preliminary experiments aimed at characterizing the pulses obtained with single and multi-ring delay masks, with ionization pulses in second harmonics and with a single-stage target, will be carried out in PW-scale laser facilities.

Methods

Generation of the driver pulse train

The envisaged setup tailored on the proposed working configuration is based upon a 200TW Ti:Sa system, delivering 4.6 J energy pulses with 25 fs duration, a collimated FWHM diameter of 100 mm and central wavelength of 810 nm. The evaluation of the properties of the laser beams in the intermediate-field or in the vicinity of their focal points is obtained by solving the Helmholtz equation in the paraxial approximation $k_0 \partial_z u = -i/2 \nabla^2 u$, where $u = E(x, y, z)$ is the pulse electric field and z is the propagation direction. A standard numerical solution of the equation at the propagation distance $u(z)$ from the parabola is obtained as $u(z) = \text{FFT}^{-1}(\hat{u}_0(k_x, k_y) \exp(-\frac{i}{2k_0}(k_x^2 + k_y^2)z))$, where k is the pulse wavenumber, $\hat{u}_0 = \text{FFT}(u_0(x, y, 0))$ is the Fast Fourier Transform (FFT) of the laser field right after the reflection from the parabola and FFT^{-1} is the inverse FFT operator.

The generation of stable double-pulse trains is assured by inserting a multi-ring structure, acting to delay different portions of the beam to each other, similar to the delay mask proposed in⁹⁹. The splitting mask considered here consists of five fused silica rings of thickness 98 μm generating two multi-ring pulse structures of the collimated beam without significantly lengthening each sub pulse (see Figs. 1a and 9a,c), where the collimated pulses distributions right after the passage through the mask are shown). From a constructive point of view, the structure can either be obtained using a thin thread acting to hold the rings together, or by considering a common substrate of the rings (thus providing an offset to the thickness of the regions travelled by the two beams undergoing the delay from each other); according to preliminary contacts with manufacturers, a safe value of $\sim 100 \mu\text{m}$ can be considered for this common substrate. Unlike the single ring tested so far¹⁰⁰, the multi-ring allows for the generation of two beams having very similar transverse distributions in the vicinity of the focus of the F/38 parabola, with tunable energy content. As it is apparent in panels b) and d) of Fig. 9, the pulses transverse distributions in the focal plane are very close to gaussian shapes with waist $w_{0,d} = 30 \mu\text{m}$, and peak intensities of $I_{d,1} = 2.8 \times 10^{18} \text{W/cm}^2$ and $I_{d,2} = 3.4 \times 10^{18} \text{W/cm}^2$ for the first and second pulse, respectively, corresponding to normalized amplitudes for the circularly polarized pulses of $a_{0,d1} = 0.81$ and $a_{0,d2} = 0.89$. The splitting mask, which includes the built-in pickup mirror, is based upon a reliable and stable method which however introduces diffraction energy losses. To evaluate them, we compare the total energy delivered by the equivalent gaussian (TEM00) pulses having 30 μm waist, duration 25 fs and peak intensities of $I_{d,1}$ and $I_{d,2}$, thus delivering a total energy in the spot of 2.02 J, with the energy of 4.04 J delivered by the equivalent TEM00 pulse obtained without the rings, thus assessing a 50.0% energy conversion in the spot of the splitting technique.

Trapping analysis for dark-current free beams

The 1D dominated trapping condition for electrons with negligible transverse momentum reads $\phi_{ex.} \geq \phi_{tr.} + 1 - 1/\gamma_{\phi}^{101}$, where $\phi_{ex.;tr.}$ are the normalized potential at the extraction and trapping points and $\phi(z) = e\varphi(z)/m_e c^2 = -k_p \int^z (E_z/E_{0,p}) dz'$. Panels a) and b) of Fig. 3 depict the details of particle extraction and trapping for the proposed working point. The *weak* or *standard* trapping condition ensures the trapping of the particles at least at the minimum of the potential (located at around $\xi = k_p(z - ct) = 3$), *i.e.* at the end of the accelerating region of the bucket⁵¹. A particularly important trapping condition, which enables the generation of ultrashort pulses²¹, is the *strong* trapping condition⁴⁷, which is satisfied when the particles are trapped at around the peak of the accelerating gradient, *i.e.* when $\phi_{tr.} = 0$. In panel b) of Fig. 3 the *weak*

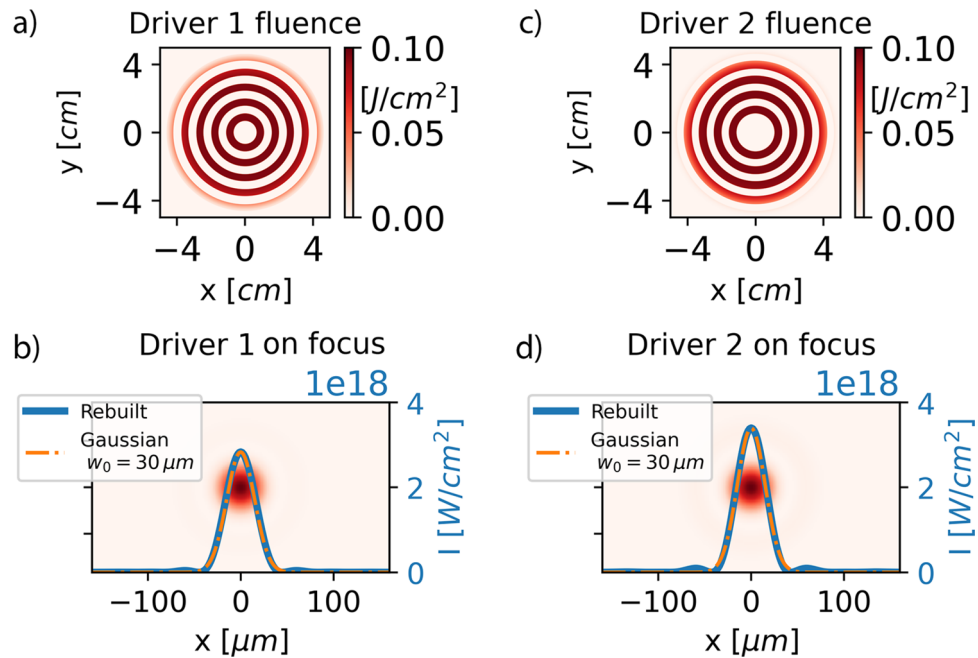


Fig. 9. Generation of the two-pulses driver train by using delay rings. The rings structure is composed by quartz rings of thickness $98\ \mu\text{m}$ glued or etched onto a transparent substrate equipped with a hole. Panels (a) and (c): After the passage through the temporal splitter, two multi-ring structures delayed by 151 fs are generated. Panels (b) and (d): In the far field, each of the two structures evolves into quasi-gaussian pulses, with minimum waist of $w_{0;d} = 30\ \mu\text{m}$.

and the more demanding *strong* conditions for the normalized potentials at the extraction points are shown as the dashed and dashed-dot lines, respectively. From that, we can infer that only particles extracted in the longitudinal region depicted by the green vertical band can be trapped (*i.e.* they will satisfy the *weak* condition), while among them only those in the red vertical band can be trapped in the vicinity of the accelerating gradient's peak (*i.e.* they will satisfy the *strong* condition). It is worth mentioning here that particles extracted off-axis necessarily will experience a smaller variation in the potential. As a result, if particles don't satisfy at least the *weak* trapping condition as inferred by the green region in panel b), they won't be trapped in the wakefield. The actual extraction regions of the electrons can be inferred by inspecting panel a) in the same figure, where the electric fields of the wakefield and of the laser are normalized to the Dawson field $E_{0,p}^{102}$ and to the $E_{0,l} = m_e c^2 / k_l$, respectively. The horizontal black and red dashed lines in panel a) show the characteristic values of the electric field in which the ionization processes $Ar^{9^+ \rightarrow 10^+}$ and $Ar^{10^+ \rightarrow 11^+}$ reach the saturation regime, respectively, while the corresponding vertical lines depict the longitudinal on-axis regions where those processes are activated. Among them, only the region around the peak of the ionization pulse is overlapping with the trapping region (see panel b), assuring us that the electrons extracted by the driver train won't be trapped by the wakefield and therefore they will not constitute a dark-current. Finally, with similar arguments, from panels a) and b) we can deduce that the selected working conditions assures the trapping of both the $Ar^{9^+ \rightarrow 10^+}$ and $Ar^{10^+ \rightarrow 11^+}$ particles extracted by the ionization pulse, and only from that, in a region close to the peak of the accelerating gradient, therefore fulfilling the *strong* trapping for all the electrons in the bunch. This is confirmed by the series of the q-3D PIC simulations we performed.

Ionization pulse generation and focusing

The ionization pulse is generated by extracting 160 mJ of energy from the main pulse using a pick-up mirror mounted along the axis of the delay mask structure. The conversion in third harmonics (see *e.g.*¹⁰³) is operated with combined Second Harmonic Generation (SHG) and Third Harmonic Generation (THG) crystals. For the SHG, a $300\ \mu\text{m}$ thick Type I LBO crystal is an ideal choice due to its high damage threshold. According to numerical simulations, for the THG, a $70\ \mu\text{m}$ thick Type I BBO crystal can ensure both high conversion efficiency and short pulse duration. The numerical results indicate that a 66 mJ, 29 fs FWHM pulse can be generated at the third-harmonic frequency if the beam diameter on the crystals is 25 mm. The ionization pulse focusing is obtained with a dedicated F/13 parabola and a holed mirror (see *Supplementary Materials* for a full description of the setup).

Minimum achievable emittance and saturation effects

The evaluation of the residual transverse momentum of the extracted electrons after the pulse passage had been developed in⁵² and recently expanded so as to include saturation and multiple processes effects⁵³, both of them being relevant for the regime explored in this work. The main parameters assessing the fraction of extracted electrons, as well as their residual momenta and emittance after the pulse passage, are the peak electric field (here

conveniently expressed as the combination of the pulse normalized amplitude $a_{0,i}$ and wavelength $\lambda_i = \lambda_d/3$, the pulse waist $w_{0,d} = 3.5 \mu\text{m}$ and FWHM duration $T_i = 30 \text{ fs}$, as well as the atomic parameters as the initial quantum state of the freshly extracted electron and its ionization potential U_I . The electric field amplitude $E(t)$ can be conveniently normalized as $\rho(t) \equiv \frac{3E(t)}{2E_a} \left(\frac{U_H}{U_I}\right)^{3/2}$ ⁴⁷, where $E_a = 5.14 \cdot 10^{11} \text{ V/m}$ is the atomic field unit and $U_H = 13.598 \text{ eV}$ is the Hydrogen ionization potential, with which the ADK ionization probability rate⁷³ can be rewritten in the simple expression $W_i(t) = C \cdot \rho^\mu(t) \exp[-1/\rho(t)]$ ⁴⁷. The exponent μ is defined as $\mu = -2n^* + |m| + 1$, being $n^* = Z(U_H/U_I)^{1/2}$ the effective quantum number and Z the ion charge after the extraction, respectively, and the multiplication factor C depends on the principal and angular quantum numbers of the electron initial state. The onset of the saturation process, *i.e.* the extraction of a significant fraction of the available electrons, is regulated by the saturation parameter

$$\bar{\nu}_s = \frac{k_{ADK} c T}{\sqrt{\ln 2}} \rho_0^{\mu+1} e^{-\frac{1}{\rho_0}} \quad (2)$$

(see Eq. 45 in⁵³), ρ_0 being the maximum pulse normalized field and $k_{ADK} = C/c$. As, after the pulse passage, the fraction $1 - e^{-\bar{\nu}_s}$ of the available electrons are extracted by the pulse, the value of $\bar{\nu}_s = 1$ sets the amount of about 63% of the extracted electrons. We can therefore identify an unsaturated regime in which $\bar{\nu}_s \ll 1$, with the saturation occurring when $\bar{\nu}_s \gtrsim 1$. At the focus point, the peak normalized electric field for a given ionization process can be evaluated as $\rho_0 = a_{0,i}/a_c$ ⁴⁷, where the critical amplitude $a_c \simeq 0.107(U_I/U_H)^{3/2} \lambda_i$ depends on the selected process. As the $Ar^{8^+ \rightarrow 9^+}$ one had been already fully saturated by the driver train, the critical amplitudes for the active ionization channels $Ar^{9^+ \rightarrow 10^+}$ and $Ar^{10^+ \rightarrow 11^+}$ are $a_{c,9 \rightarrow 10} = 6.05$ and $a_{c,10 \rightarrow 11} = 7.21$, respectively, leading to the normalized maximum fields of the ionization pulse of $\rho_{9 \rightarrow 10} = 0.0633$ and $\rho_{10 \rightarrow 11} = 0.0532$. The number of extracted electrons from the next process is negligible, as confirmed by both PIC simulations and by theory⁵³. The subsequent evaluation of the saturation parameters $\bar{\nu}_s$ at the focus point of the ionization pulse reads $\bar{\nu}_{s,9 \rightarrow 10} = 13$ and $\bar{\nu}_{s,10 \rightarrow 11} = 1.4$, meaning that 100% of the $Ar^{9^+ \rightarrow 10^+}$ and nearly 75% of the $Ar^{10^+ \rightarrow 11^+}$ electrons are extracted on axis at the focus point.

The residual transverse momentum after the pulse slippage gets contribution both from the non zero laser potential at the extraction point and from the radial ponderomotive effects. The latter, being directly proportional to the radial coordinate, does not directly contribute to the increase of the beam emittance and it can be evaluated as $\sigma(u_{PF,x}) = \sigma(u_{PF,y}) \approx \sqrt{\pi \rho_0 / \ln(4)} (a_{0,i}^2/4) (cT/w_{0,i}) < 5 \cdot 10^{-3}$ in our selected working point (see Eq. 15 and 22 in Ref.⁵², where $\Delta = \sqrt{\rho_0}$). The ponderomotive contribution to the residual momentum turns out to be negligible with respect to the extraction phase effect $\sigma(u_x) \approx \sqrt{\rho_0} a_{0,i} \approx 10^{-1}$ (see Eq. 10 in⁵²). The evaluation of the minimum attainable transverse emittance along the ionization pulse polarization plane, obtained with the results from Eq. 42 in⁵³, resulted in a minimum value of $\epsilon_{n,x}|_{min} \simeq 60 \text{ nm}$, which is about 30% less than the one observed in the PIC simulations (see the *Supplementary Materials* document). However, the evolution in time of the beam momenta and size right after the beam slippage includes space-charge and wakefield effects, the former becoming negligible only once the electrons become ultrarelativistic. Nonlinearities in the radial focusing field $F_r = E_r - B_\phi$, and/or longitudinal gradients in the radial field strength $K(\xi) = k_p \partial_r F_r$ also induce an increase in the projected emittance, which at the trapping point is expected to be higher than the one evaluated right after the extraction and the pulse slippage.

Particle-in-cell simulations of electron acceleration

The Particle In Cell simulations were obtained with the FBPIC code¹⁰⁴, which enforces a quasi-3D geometry and employs a tunnel ionization module with ADK formula as in¹⁰⁵. Convergence scans were conducted in order to assess the numerical stability and accuracy of the numerical results presented in the paper. The radial resolution $dr = 25 \text{ nm}$ was set in order to resolve the beam current density also at late stages of the acceleration process, where the matched beam radial size reduced to a geometrical mean FWHM diameter of about 150 nm. Moreover, due to the necessity of spatially resolving the field ionization process, occurring around the ionization pulse electric field peaks and with longitudinal extension of $\delta z_{ion} \simeq \sqrt{\rho_0} \lambda_i / 2 \simeq 40 \text{ nm}$, a longitudinal resolution of $dz = 10 \text{ nm}$ was set. This is consistent with the necessity of longitudinally resolving the beam current density, having a FWHM length of about 180 nm. Finally, the angular projection on three azimuthal modes was employed, in order to accurately describe the beam-loading effects. The particle deposition was with $Nz \times Nr \times Nt = 2 \times 1 \times 12 = 24 \text{ ppc}$, with the exemption of a cylinder of radius $0.5 \times w_{0,i}$ inside the injection section, where a deposition of $Nz \times Nr \times Nt = 4 \times 4 \times 24 = 384 \text{ ppc}$ was adopted so as to improve the numerical accuracy of the trapped beam density current. Simulations ran on 32xH100 GPU's at ELI-NP cluster. To speed-up the run-time, a Lorentz boost frame technique^{106,107} with boost $\gamma_{boost} = 10$ was employed in all the simulations. The chosen value for γ_{boost} was obtained by pondering the runtime (about 35 h/simulation) and the increase of the beam particle's weights, which induces a degradation of the beam density current numerical description. The time-step increase was $dt = 4.59 \text{ as}$, so as to ensure the stability of the results against numerical Cerenkov radiation (NCR) noise due to the boosted-frame technique.

Data availability

All data needed to evaluate the conclusions in the paper are present in the paper. Simulation results are available from the corresponding author upon reasonable request.

Received: 25 June 2025; Accepted: 14 October 2025

Published online: 19 November 2025

References

- Tajima, T. & Dawson, J. M. Laser electron accelerator. *Phys. Rev. Lett.* **43**, 267 (1979).
- Esarey, E., Schroeder, C. B. & Leemans, W. P. Physics of laser-driven plasma-based electron accelerators. *Rev. Mod. Phys.* **81**, 1229 (2009).
- Esarey, E., Shadwick, B., Catravas, P. & Leemans, W. Synchrotron radiation from electron beams in plasma-focusing channels. *Phys. Rev. E* **65**, 056505 (2002).
- Schlenvoigt, H.-P. et al. A compact synchrotron radiation source driven by a laser-plasma wakefield accelerator. *Nat. Phys.* **4**, 130–133 (2008).
- Kneip, S. et al. X-ray phase contrast imaging of biological specimens with femtosecond pulses of betatron radiation from a compact laser plasma wakefield accelerator. *Appl. Phys. Lett.* **99** (2011).
- Fourmaux, S. et al. Single shot phase contrast imaging using laser-produced betatron x-ray beams. *Opt. Lett.* **36**, 2426–2428 (2011).
- Guo, B. et al. High-resolution phase-contrast imaging of biological specimens using a stable betatron x-ray source in the multiple-exposure mode. *Sci. Rep.* **9**, 7796 (2019).
- Glinec, Y. et al. Radiotherapy with laser-plasma accelerators: Monte carlo simulation of dose deposited by an experimental quasimonoenergetic electron beam. *Med. Phys.* **33**, 155–162 (2006).
- Nicolai, M. et al. Realizing a laser-driven electron source applicable for radiobiological tumor irradiation. *Appl. Phys. B* **116**, 643–651 (2014).
- Labate, L. et al. Toward an effective use of laser-driven very high energy electrons for radiotherapy: Feasibility assessment of multi-field and intensity modulation irradiation schemes. *Sci. Rep.* **10**, 17307 (2020).
- Guénot, D. et al. Relativistic electron beams driven by kHz single-cycle light pulses. *Nat. Photonics* **11**, 293–296. <https://doi.org/10.1038/nphoton.2017.46> (2017).
- Gustas, D. et al. High-charge relativistic electron bunches from a KHz laser-plasma accelerator. *Phys. Rev. Accelerat. Beams* **21**, 013401. <https://doi.org/10.1103/PhysRevAccelBeams.21.013401> (2018).
- Papp, D., Léczy, Z., Kamperidis, C. & Hafz, N. A. Highly efficient few-cycle laser wakefield electron accelerator. *Plasma Phys. Control. Fusion* **63**, 065019 (2021).
- Horný, V., Bleout, P., Ursescu, D., Malka, V. & Tomassini, P. Efficient laser wakefield accelerator in pump depletion dominated bubble regime. *Phys. Rev. E* **110**, 035202 (2024).
- Hooker, S. et al. Multi-pulse laser wakefield acceleration: A new route to efficient, high-repetition-rate plasma accelerators and high flux radiation sources. *J. Phys. B: At. Mol. Opt. Phys.* **47**, 234003 (2014).
- Jakobsson, O., Hooker, S. & Walczak, R. GeV-scale accelerators driven by plasma-modulated pulses from kilohertz lasers. *Phys. Rev. Lett.* **127**, 184801 (2021).
- Tooley, M. et al. Towards attosecond high-energy electron bunches: Controlling self-injection in laser-wakefield accelerators through plasma-density modulation. *Phys. Rev. Lett.* **119**, 044801 (2017).
- Kornaszewski, A. et al. Plasma density shaping for attosecond electron bunch generation. In *Relativistic Plasma Waves and Particle Beams as Coherent and Incoherent Radiation Sources III*, vol. 11036, 77–86 (SPIE, 2019).
- Zhu, X.-L. et al. Generation of 100-MeV attosecond electron bunches with terawatt few-cycle laser pulses. *Phys. Rev. Appl.* **15**, 044039. <https://doi.org/10.1103/PhysRevApplied.15.044039> (2021).
- Ferri, J., Horný, V. & Fülöp, T. Generation of attosecond electron bunches and x-ray pulses from few-cycle femtosecond laser pulses. *Plasma Phys. Controlled Fusion* **63**, 045019. <https://doi.org/10.1088/1361-6587/abe885> (2021).
- Tomassini, P., Horný, V. & Doria, D. Attosecond pulses from ionization injection wakefield accelerators. *Instruments* **7**, 34 (2023).
- Nakajima, K. Towards a table-top free-electron laser. *Nat. Phys.* **4**, 92–93 (2008).
- Nghiêm, P. et al. Toward a plasma-based accelerator at high beam energy with high beam charge and high beam quality. *Phys. Rev. Accelerat. Beams* **23**, 031301 (2020).
- Assmann, R. et al. Eupraxia conceptual design report. *Eur. Phys. J. Special Topics* **229**, 3675–4284 (2020).
- Emma, C. et al. Free electron lasers driven by plasma accelerators: Status and near-term prospects. *High Power Laser Sci. Eng.* **9**, e57 (2021).
- Wang, W. et al. Free-electron lasing at 27 nanometres based on a laser wakefield accelerator. *Nature* **595**, 516–520 (2021).
- Bemporad, C., Milburn, R. H., Tanaka, N. & Fotino, M. High-energy photons from Compton scattering of light on 6.0-GeV electrons. *Phys. Rev.* **138**, B1546 (1965).
- Esarey, E., Ride, S. K. & Sprangle, P. Nonlinear Thomson scattering of intense laser pulses from beams and plasmas. *Phys. Rev. E* **48**, 3003 (1993).
- Catravas, P., Esarey, E. & Leemans, W. Femtosecond x-rays from Thomson scattering using laser wakefield accelerators. *Meas. Sci. Technol.* **12**, 1828 (2001).
- Tomassini, P., Giuliotti, A., Giuliotti, D. & Gizzi, L. Thomson backscattering x-rays from ultra-relativistic electron bunches and temporally shaped laser pulses. *Appl. Phys. B* **80**, 419–436 (2005).
- Tomassini, P. et al. High-quality electron bunch production for high-brilliance Thomson scattering sources. In *Laser Acceleration of Electrons, Protons, and Ions IV*, vol. 10240, 81–98 (SPIE, 2017).
- Kaganovich, D. et al. First demonstration of a staged optical injection and laser wakefield acceleration. In *Quantum Electronics and Laser Science Conference, JWD3* (Optica Publishing Group, 2005).
- Steinke, S. et al. Staging of laser-plasma accelerators. *Phys. Plasmas* **23**, 056705. <https://doi.org/10.1063/1.4948280> (2016). https://pubs.aip.org/aip/pop/article-pdf/doi/10.1063/1.4948280/15946431/056705_1_online.pdf
- Lindström, C. A. Staging of plasma-wakefield accelerators. *Phys. Rev. Accel. Beams* **24**, 014801. <https://doi.org/10.1103/PhysRevAccelBeams.24.014801> (2021).
- Pathak, N., Zhidkov, A. & Hosokai, T. Electron beam chirp dexterity in staging laser wakefield acceleration. *Phys. Plasmas* **28**, 053105. <https://doi.org/10.1063/5.0040897> (2021).
- Report on the Advanced Linear Collider Study Group (ALEGRO) Workshop 2024*. [arXiv:2408.03968](https://arxiv.org/abs/2408.03968).
- Bulanov, S., Naumova, N., Pegoraro, F. & Sakai, J. Particle injection into the wave acceleration phase due to nonlinear wake wave breaking. *Phys. Rev. E* **58**, R5257 (1998).
- Tomassini, P. et al. Production of high-quality electron beams in numerical experiments of laser wakefield acceleration with longitudinal wave breaking. *Phys. Rev. ST Accel. Beams* **6**, 121301. <https://doi.org/10.1103/PhysRevSTAB.6.121301> (2003).
- Brantov, A. et al. Controlled electron injection into the wake wave using plasma density inhomogeneity. *Phys. Plasmas* **15** (2008).
- Gonsalves, A. et al. Tunable laser plasma accelerator based on longitudinal density tailoring. *Nat. Phys.* **7**, 862–866 (2011).
- Buck, A. et al. Shock-front injector for high-quality laser-plasma acceleration. *Phys. Rev. Lett.* **110**, 185006 (2013).
- Ekerfelt, H., Hansson, M., Gallardo González, I., Davoine, X. & Lundh, O. A tunable electron beam source using trapping of electrons in a density down-ramp in laser wakefield acceleration. *Sci. Rep.* **7**, 12229 (2017).
- Ke, L. et al. Near-GeV electron beams at a few per-mille level from a laser wakefield accelerator via density-tailored plasma. *Phys. Rev. Lett.* **126**, 214801 (2021).
- Grafenstein, K. V. et al. Laser-accelerated electron beams at 1 GeV using optically-induced shock injection. *Sci. Rep.* **13**, 11680 (2023).
- Yu, L.-L. et al. Two-color laser-ionization injection. *Phys. Rev. Lett.* **112**, 125001 (2014).

46. Schroeder, C. et al. Ultra-low emittance beam generation using two-color ionization injection in laser-plasma accelerators. In *Laser Acceleration of Electrons, Protons, and Ions III; and Medical Applications of Laser-Generated Beams of Particles III*, vol. 9514, 8–14 (SPIE, 2015).
47. Tomassini, P. et al. The resonant multi-pulse ionization injection. *Phys. Plasmas*. **24** (2017).
48. Schroeder, C., Benedetti, C., Esarey, E., Chen, M. & Leemans, W. Two-color ionization injection using a plasma beatwave accelerator. *Nucl. Instrum. Methods Phys. Res., Sect. A* **909**, 149–152 (2018).
49. Tomassini, P. et al. High quality electron bunches for a multistage GeV accelerator with resonant multipulse ionization injection. *Phys. Rev. Accelerat. Beams* **22**, 111302 (2019).
50. Tomassini, P. et al. High-quality 5 GeV electron bunches with resonant multi-pulse ionization injection. *Plasma Phys. Control. Fusion* **62**, 014010 (2019).
51. Esarey, E. & Pilloff, M. Trapping and acceleration in nonlinear plasma waves. *Phys. Plasmas*. **2**, 1432–1436. <https://doi.org/10.1063/1.871358> (1995).
52. Schroeder, C. et al. Thermal emittance from ionization-induced trapping in plasma accelerators. *Phys. Rev. Special Topics-Accelerat. Beams* **17**, 101301 (2014).
53. Tomassini, P., Massimo, F., Labate, L. & Gizzi, L. A. Accurate electron beam phase-space theory for ionization-injection schemes driven by laser pulses. *High Power Laser Sci. Eng.* **10**, e15 (2022).
54. Zholents, A. A. & Fawley, W. M. Proposal for intense attosecond radiation from an x-ray free-electron laser. *Phys. Rev. Lett.* **92**, 224801 (2004).
55. Marinelli, A. et al. Experimental demonstration of a single-spike hard-x-ray free-electron laser starting from noise. *Appl. Phys. Lett.* **111** (2017).
56. Franz, P. et al. Terawatt-scale attosecond x-ray pulses from a cascaded superradiant free-electron laser. *Nat. Photonics* **18**, 698–703 (2024).
57. Tomassini, P. et al. Linear and nonlinear Thomson scattering for advanced x-ray sources in PLASMONX. *IEEE Trans. Plasma Sci.* **36**, 1782–1789 (2008).
58. Maroli, C., Petrillo, V., Tomassini, P. & Serafini, L. Nonlinear effects in thomson backscattering. *Phys. Rev. Special Topics-Accelerat. Beams* **16**, 030706 (2013).
59. Kaganovich, D. et al. High efficiency guiding of terawatt subpicosecond laser pulses in a capillary discharge plasma channel. *Phys. Rev. E* **59**, R4769 (1999).
60. Bobrova, N., Bulanov, S., Esaulov, A. & Sasorov, P. Capillary discharges for guiding of laser pulses. *Plasma Phys. Rep.* **26**, 10–20 (2000).
61. Cros, B. et al. Eigenmodes for capillary tubes with dielectric walls and ultraintense laser pulse guiding. *Phys. Rev. E* **65**, 026405 (2002).
62. Veysman, M. & Andreev, N. Comparative study of laser pulses guiding in capillary waveguides and plasma channels at conditions of non-perfect focusing. In *Journal of Physics: Conference Series*, vol. 774, 012109 (IOP Publishing, 2016).
63. Gonsalves, A. J. et al. Laser-heated capillary discharge plasma waveguides for electron acceleration to 8 GeV. *Phys. Plasmas*. **27** (2020).
64. Li, J.-L. et al. Generation of a curved plasma channel from a discharged capillary for intense laser guiding. *High Power Laser Sci. Eng.* **11**, e58 (2023).
65. Shaloo, R. J. et al. Hydrodynamic optical-field-ionized plasma channels. *Phys. Rev. E* **97**, 053203 (2018).
66. Shaloo, R. et al. Low-density hydrodynamic optical-field-ionized plasma channels generated with an axicon lens. *Phys. Rev. Accelerat. and Beams* **22**, 041302 (2019).
67. Alejo, A., Cowley, J., Picksley, A., Walczak, R. & Hooker, S. Demonstration of kilohertz operation of hydrodynamic optical-field-ionized plasma channels. *Phys. Rev. Accelerat. and Beams* **25**, 011301 (2022).
68. Picksley, A. et al. Matched guiding and controlled injection in dark-current-free, 10-gev-class, channel-guided laser-plasma accelerators. *Phys. Rev. Lett.* **133**, 255001 (2024).
69. Li, R. et al. Longitudinal tapering in gas jets for increased efficiency of 10-GeV class laser plasma accelerators. *Rev. Sci. Instrum.* **96** (2025).
70. Esarey, E., Sprangle, P., Krall, J. & Ting, A. Self-focusing and guiding of short laser pulses in ionizing gases and plasmas. *IEEE J. Quantum Electron.* **33**, 1879–1914. <https://doi.org/10.1109/3.641305> (1997).
71. Schroeder, C. B., Esarey, E., Shadwick, B. A. & Leemans, W. P. Trapping and dark current in plasma-based accelerators. *AIP Conf. Proc.* **737**, 564–570. <https://doi.org/10.1063/1.1842592> (2004).
72. Perelomov, A., Popov, V. & Terent'ev, M. Ionization of atoms in an alternating electric field. *Sov. Phys. JETP* **23**, 924–934 (1966).
73. Amosov, M. & Delone, N. Tunnel ionization of complex atoms and atomic ions in electromagnetic field. In *Proc. SPIE* **664**, 138–140 (1986).
74. Yudin, G. L. & Ivanov, M. Y. Nonadiabatic tunnel ionization: Looking inside a laser cycle. *Phys. Rev. A* **64**, 013409 (2001).
75. Pukhov, A. & Meyer-ter Vehn, J. Laser wake field acceleration: The highly non-linear broken-wave regime. *Appl. Phys. B* **74**, 355–361 (2002).
76. Sprangle, P., Esarey, E. & Ting, A. Nonlinear interaction of intense laser pulses in plasmas. *Phys. Rev. A* **41**, 4463 (1990).
77. Mehrling, T., Grebenyuk, J., Tsung, F., Floettmann, K. & Osterhoff, J. Transverse emittance growth in staged laser-wakefield acceleration. *Phys. Rev. Special Topics-Accelerat. Beams* **15**, 111303 (2012).
78. Floettmann, K. Adiabatic matching section for plasma accelerated beams. *Phys. Rev. Special Topics-Accelerat. Beams* **17**, 054402 (2014).
79. Tomassini, P. & Rossi, A. Matching strategies for a plasma booster. *Plasma Phys. Control. Fusion* **58**, 034001 (2015).
80. Kondratenko, A. & Saldin, E. Generating of coherent radiation by a relativistic electron beam in an undulator. *Part. Accel.* **10**, 207–216 (1980).
81. Bonifacio, R., Pellegrini, C. & Narducci, L. Collective instabilities and high-gain regime in a free electron laser. *Opt. Commun.* **50**, 373–378 (1984).
82. Dattoli, G., Del Franco, M., Labat, M., Ottaviani, P. & Pagnutti, S. Introduction to the physics of free electron laser and comparison. *Free Electron Lasers 1* (2012).
83. Pellegrini, C., Marinelli, A. & Reiche, S. The physics of x-ray free-electron lasers. *Rev. Mod. Phys.* **88**, 015006 (2016).
84. Hidding, B. et al. Ultracold electron bunch generation via plasma photocathode emission and acceleration in a beam-driven plasma blowout. *Phys. Rev. Lett.* **108**, 035001 (2012).
85. Golovanov, A., Kostyukov, I. Y., Thomas, J. & Pukhov, A. Analytic model for electromagnetic fields in the bubble regime of plasma wakefield in non-uniform plasmas. *Phys. Plasmas*. **24** (2017).
86. Wang, W. et al. High-brightness high-energy electron beams from a laser wakefield accelerator via energy chirp control. *Phys. Rev. Lett.* **117**, 124801 (2016).
87. Xu, X. et al. Generation of ultrabright and low energy spread electron beams in laser wakefield acceleration in a uniform plasma. *Phys. Rev. Accelerat. Beams* **26**, 111302 (2023).
88. Tanaka, K. et al. Current status and highlights of the ELI-NP research program. *Matter Radiat. Extremes* **5** (2020).
89. Rus, B. et al. ELI-Beamlines: progress in development of next generation short-pulse laser systems. In *Research Using Extreme Light: Entering New Frontiers with Petawatt-Class Lasers III*, vol. 10241, 14–21 (SPIE, 2017).

90. Yao, W. et al. Characterization and performance of the Apollon main short-pulse laser beam following its commissioning at 2 PW level. *Phys. Plasmas*. **32** (2025).
91. Sung, J. H. et al. 4.2 PW, 20 fs Ti:sapphire laser at 0.1 Hz. *Opt. Lett.* **42**, 2058–2061 (2017).
92. <https://nsf-opal.rochester.edu>.
93. Di Piazza, A., Willingale, L. & Zuegel, J. Multi-petawatt physics prioritization (MP3) workshop report. [arXiv:2211.13187](https://arxiv.org/abs/2211.13187) (2022).
94. Di Piazza, A. First-order strong-field QED processes in a tightly focused laser beam. *Phys. Rev. A* **95**, 032121 (2017).
95. Di Piazza, A., Müller, C., Hatsagortsyan, K. & Keitel, C. H. Extremely high-intensity laser interactions with fundamental quantum systems. *Rev. Mod. Phys.* **84**, 1177–1228 (2012).
96. Yan, W. et al. High-order multiphoton Thomson scattering. *Nat. Photonics* **11**, 514–520 (2017).
97. Vyskočil, J., Gelfer, E. & Klimo, O. Inverse Compton scattering from solid targets irradiated by ultra-short laser pulses in the 10^{22} – 10^{23} W/cm² regime. *Plasma Phys. Controlled Fusion* **62**, 064002 (2020).
98. Mirzaie, M. et al. All-optical nonlinear Compton scattering performed with a multi-petawatt laser. *Nat. Photonics* **18**, 1212–1217 (2024).
99. Vantaggiato, G., Labate, L., Tomassini, P. & Gizzi, L. Modelling of pulse train generation for resonant laser wakefield acceleration using a delay mask. *Nucl. Inst. Methods Phys. Res. A* **909**, 114–117 (2018).
100. Marasciulli, A., Labate, L., Tomassini, P. & Gizzi, L. Signatures of resonantly driven laser-wakefield excitation by a pulse train generated by an optical delay mask. *Appl. Opt.* **62**, 9368 (2023).
101. Khachatryan, A. G. Trapping, compression, and acceleration of an electron bunch in the nonlinear laser wakefield. *Phys. Rev. E* **65**, 046504 (2002).
102. Dawson, J. M. Nonlinear electron oscillations in a cold plasma. *Phys. Rev.* **113**, 383 (1959).
103. Fan-Chiang, L. et al. Third harmonic generation for two-color ionization injection in laser-plasma accelerators. In *2022 IEEE Advanced Accelerator Concepts Workshop (AAC)*, 1–3 (IEEE, 2022).
104. Lehe, R., Kirchen, M., Andriyash, I. A., Godfrey, B. B. & Vay, J.-L. A spectral, quasi-cylindrical and dispersion-free particle-in-cell algorithm. *Comput. Phys. Commun.* **203**, 66–82 (2016).
105. Chen, M. et al. Numerical modeling of laser tunneling ionization in explicit particle-in-cell codes. *J. Comput. Phys.* **236**, 220–228. <https://doi.org/10.1016/j.jcp.2012.11.029> (2013).
106. Vay, J.-L. Noninvariance of space-and time-scale ranges under a Lorentz transformation? format? and the implications for the study of relativistic interactions. *Phys. Rev. Lett.* **98**, 130405 (2007).
107. Kirchen, M. et al. Stable discrete representation of relativistically drifting plasmas. *Phys. Plasmas*. **23**, 100704. <https://doi.org/10.1063/1.4964770> (2016).

Acknowledgements

P.T. thanks the invaluable support from A. Berceanu (ELI-NP/LGED) and from the ELI-NP IT department, in particular from M. Ciubancan, M.I. Isverceanu and D. Zabet, for the ELI-NP cluster configuration.

Author contributions

P.T. make the work conceptualization, the PIC simulations and drafted the manuscript; F.A. made the pulse propagation simulations and revised the manuscript; N.H. and S.T. designed the ionization pulse conversion set-up and revised the manuscript; V.H. revised the manuscript; L.L. contributed to the pulse time splitting concept and revised the manuscript; D.D. revised the proposed experimental setup; L.G. made the conceptualization of the ionization pulse focusing, contributed to the splitting pulse design, revised the manuscript and the proposed experimental setup.

Funding

The Extreme Light Infrastructure Nuclear Physics (ELI-NP) team acknowledges the support of the Romanian Government and the European Union through the European Regional Development Fund - the Competitiveness Operational Programme (1/07.07.2016, COP, ID 1334) Phases II, and the Romanian Ministry of Research, Innovation and Digitalization: Program Nucleu PN23210105. Accessing the ELI-NP facility is supported by the IOSIN funds for research infrastructures of national interest funded by the Romanian Ministry of Research, Innovation and Digitalization. Authors draw support also from the ELI-RO contracts ELI-RO/RDI/2024 14 SPARC and ELI-RO/RDI/2024 2024 008 AMAP funded by PN III/P5/Subprogram 5.1. We acknowledge EuroHPC Joint Undertaking for awarding us access to Karolina at IT4Innovations (VŠB-TU), Czechia under project number EHPC-REG-2025R01-007 (EU-25-87); Ministry of Education, Youth and Sports of the Czech Republic through the e-INFRA CZ (ID:90140). We also acknowledge contributions from the Integrated Infrastructure Initiative in Photonic and Quantum Sciences (I-PHOQS, CUP B53C22001750006, ID D2B8D520, IR0000016) and Tuscany Health Ecosystem (THE)-Spoke 1: Advanced Radiotherapies and Diagnostics in Oncology (ECS00000017, D.D. MUR No. 1055 23 May 2022) funded by the NextGenerationEU (PNRR-Italy), EuPRAXIA Advanced Photon Sources–EuAPS (CUP I93C21000160006, IR0000030), the Horizon 2020 Framework Programme Research and Innovation and Program EuPRAXIA Preparatory Phase (No. 101079773).

Declarations

Competing interests

The authors declare no competing interests.

Additional information

Supplementary Information The online version contains supplementary material available at <https://doi.org/10.1038/s41598-025-24672-7>.

Correspondence and requests for materials should be addressed to P.T.

Reprints and permissions information is available at www.nature.com/reprints.

Publisher's note Springer Nature remains neutral with regard to jurisdictional claims in published maps and institutional affiliations.

Open Access This article is licensed under a Creative Commons Attribution-NonCommercial-NoDerivatives 4.0 International License, which permits any non-commercial use, sharing, distribution and reproduction in any medium or format, as long as you give appropriate credit to the original author(s) and the source, provide a link to the Creative Commons licence, and indicate if you modified the licensed material. You do not have permission under this licence to share adapted material derived from this article or parts of it. The images or other third party material in this article are included in the article's Creative Commons licence, unless indicated otherwise in a credit line to the material. If material is not included in the article's Creative Commons licence and your intended use is not permitted by statutory regulation or exceeds the permitted use, you will need to obtain permission directly from the copyright holder. To view a copy of this licence, visit <http://creativecommons.org/licenses/by-nc-nd/4.0/>.

© The Author(s) 2025